

Final Technical Report

USGS NEHRP Grant 07HQGR0046

Three-dimensional models of crustal structure in eastern North America

James B. Gaherty¹, Colleen Dalton², and Vadim Levin³

¹*Principal Investigator*

Lamont-Doherty Earth Observatory
Columbia University
61 Route 9W
Palisades, NY 10964
Ph. (845) 365-8450
Fax (845) 365-8150
Email: Gaherty@LDEO.columbia.edu

²Dept of Earth Sciences
Boston University
675 Commonwealth Ave
Boston, MA 02215, USA
Ph. (617) 358-5433
Fax (617) 353-3290
Email: Dalton@bu.edu

³Dept of Earth and Planetary Sciences
Rutgers University
610 Taylor Road
Piscataway, NJ 08854
Ph. (732) 445-2435
Fax (732) 445-3374
Email: vlevin@rci.rutgers.edu

Term of Award: Jan 1, 2007 – Jan 1, 2009 (including no-cost extension)

Abstract. We present three-dimensional models of crustal structure for the central and eastern United States (CEUS), east of 100°W longitude. These 3D wavespeed models are derived from two types of observables measured on broadband seismic recordings from 72 stations of the Advanced National Seismic System (ANSS): (1) Rayleigh waveforms in the period range 8-30 s propagating between all possible pairs of stations in the region, generated through cross-correlation of ground-motion noise (so-called ambient-noise Green's functions); and (2) converted-phase (receiver-function) measurements beneath approximately the same set of broadband seismic stations, which provide localized estimates of integrated velocity structure between the surface and Moho beneath each station. We constructed ambient-noise Green's functions from one year of data, producing Rayleigh waveforms for nearly 1500 receiver-receiver paths with sufficient signal-to-noise ratio (> 5) for group-velocity analysis, and we have generated *Ps* receiver functions for over 45 stations. We inverted these data for a crustal model with *P* and *S* velocities defined in three layers (sediment, upper crust, and lower crust) on a 0.5x0.5 degree grid, using an averaged version of model Crust 2.0 as a starting model. Basement depth ranges from 0-13 km, while Moho depth varies from 26-50 km. Shear velocities in the sediment layer are approximately 1580 m/s, while shear velocities in the middle and lower crust average approximately 3710 and 3900 m/s, respectively. This simply parameterized and highly flexible model characterizes lateral variations in crustal structure within the CEUS in a form that is useful for earthquake source studies. The new model is available to the earthquake modeling community through the website for the Lamont Doherty Earth Observatory, specifically at http://www.ldeo.columbia.edu/~gaherty/ceus_model.

1. Introduction

Modern technologies for determining earthquake source characteristics such as event depth and moment tensor involve accurately modeling seismic waveforms, where synthetic seismograms and/or structural Green's functions are used to account for the propagation between the source and receivers. For large events ($M_w > \sim 5$) that excite high-amplitude, low-frequency ($f < 0.03$ Hz) arrivals, this analysis can be performed on a global scale using very rudimentary knowledge of crustal structure [e.g. *Dziewonski et al.*, 1981]. Detailed characterization of smaller ($M_w \sim 3.5-5$) events requires accurate knowledge of crustal shear and compressional seismic velocities for the interpretation of seismograms recorded across a broad frequency spectrum at local and regional distances [e.g. *Dreger and Helmberger*, 1993; *Ritsema and Lay*, 1993; *Zhao and Helmberger*, 1994; *Pasyanos et al.*, 1996; *Du et al.*, 2003; *Kim*, 2003; *Chen et al.*, 2005]. In tectonically active areas of the western US, the availability of dense, high-quality broadband networks and numerous local earthquake sources provides the data necessary for the construction of high-resolution regional crustal velocity models [e.g. *Magistrale et al.*, 2000; *Chen et al.*, 2007]. This has allowed regional source analyses to push to ever-smaller events, providing much more detailed pictures of regional stress and faulting characteristics [*Chen et al.*, 2008].

In the eastern US, where dense local networks are not generally available, this source characterization relies on relatively sparse recordings at regional epicentral distances [e.g. *Ammon et al.*, 1998; *Maceira et al.*, 2000; *Du et al.*, 2003; *Kim*, 2003; www.eas.slu.edu/Earthquake_Center/NM/]. Detailed regional crustal velocity models are rarely available in such regions, and most studies utilize simple one-dimensional models of the crust and upper mantle. These 1D regional models are sufficiently accurate to characterize propagation only within a relatively low-frequency band ($f < \sim 0.05$ Hz), which places a lower limit to the magnitude of events that can be analyzed, and therefore restricts the number of events that can be characterized. It is difficult to improve on these crustal models using traditional structural analysis of earthquake signals, due to the paucity of events in the region.

We present a new three-dimensional model of crustal structure in the Central and Eastern United States (CEUS), derived from joint inversion of two sets of seismic observations that are sensitive to local and regional crustal structure. The first type of observation is group-velocity estimates from Rayleigh waveforms in the period range 7-30 s propagating between all possible pairs of stations in the region, generated through cross-correlation of ground-motion noise -- so-called ambient-noise Green's functions [e.g. *Shapiro and Campillo*, 2004; *Shapiro et al.*, 2005; *Benson et al.*, 2007; *Dalton et al.*, 2011]. These data are complemented by travel times of Ps converted phases (receiver functions) measured beneath approximately the same set of broadband seismic stations, which provide localized estimates of integrated velocity structure between the surface and Moho beneath each station.

2. Ambient-Noise Rayleigh Waves

Our primary constraint on crustal velocities is derived from Rayleigh-wave group-velocity measurements from ambient-noise Green's functions. We are interested in an improved velocity model for stable central and eastern North America, and we limited

our data collection to broadband seismic stations east of longitude 100°W (Figure 1). Our analysis requires approximately one year of continuous (or nearly so) vertical-component ground-motion time series, sampled at 1-40 Hz in day-long segments. These data are derived from all available broadband stations of the Advanced National Seismographic Stations (ANSS) network, supplemented by three additional sources: the Lamont-Doherty Cooperative Seismographic Network (LCSN); the Cooperative New Madrid Seismographic Network (CNMSN); and several stations of the Canadian National Seismic Network (CNSN). The data were collected from the Data Management Center operated by the Incorporated Research Institutions for Seismology (IRIS DMC). We evaluated a number of additional regional broadband networks, as well as additional stations of the CNSN, but the requirement of nearly continuous 24-hour segments with sample rates of 40 Hz or less restricted us to the selected stations. The requested data span the 2006 calendar year, at 75 stations.

Our processing scheme closely follows that suggested by *Bensen et al.* [2007]. Time series that were continuous for approximately a full day were filtered with a zero-phase filter with corners at 5- and 50-s period, deconvolved to displacement, and downsampled to 1 Hz. Each trace was then 1-bit normalized to remove high-amplitude (earthquake) signals, and their spectrum was gently whitened. Cross-correlation functions were calculated between every station pair for which the data overlap is greater than ~80%. These daily cross-correlograms were windowed in a 4-hour window around zero lag, and then stacked into monthly stacks for each pair. Monthly stacks allowed us to assess azimuthal and seasonal variation in amplitude of the correlation peak, as well as evaluate the “symmetry” present in the correlation time series. The final stacks for year 2006 were constructed from monthly stacks weighted by completeness (number of days in each monthly stack), followed by folding the acausal and causal signals into a single average time series. This processing resulted in year-long stacks for 1855 station pairs incorporating 63 stations.

These time series provide an approximation of the ambient-noise Green’s function between the two stations [e.g. *Shapiro and Campillo, 2004; Shapiro et al., 2005*], and the dominant arrival on these vertical-component stacks can be interpreted as an interstation fundamental-mode Rayleigh wave (Figure 2). We characterize the signal-to-noise ratio (SNR) of these time series by comparing the peak amplitude within the Rayleigh-wave window (group velocity of 2.5-4.5 km/s) to the root-mean-square amplitude well outside this window. In general, SNR of the Rayleigh waveforms is inversely correlated with interstation distance (Figure 3), although there are many stations with modest separation that exhibit poor SNR. Presumably this lack of correlation results from localized noise at one or both of the stations, perhaps due to site conditions. Once corrected for the distance dependence, the SNR also displays a subtle azimuthal pattern, with highest SNR at ESE-WSW interstation azimuths. (Figure 3) This is consistent with noise sources originating along the northeast coast, most likely wave-induced microseism from the North Atlantic.

An analysis of the power spectra of the correlation functions confirms the microseism as the dominant ambient-noise source. In general, the one-bit normalization followed by whitening produces time series with relatively flat power spectra within the band of interest. The stacking process enhances the coherent portion of the signal [e.g. *Harmon et al., 2007*], and the strong peaks associated with the microseism (~7-s and ~14-s

periods) re-emerge in the power spectra of the stacked correlograms (Figure 4). Our group-velocity analysis of the Rayleigh waveforms focuses on the 6-9 and 14-30 s bands, and we avoid the spectral hole between 9-14 s period. As shown below, group-velocity measurements within these bands provide good sensitivity to shear-wave velocities throughout the crust.

Careful inspection and testing suggest that we cannot robustly estimate group velocity for waveforms with signal-to-noise ratios of less than approximately 5. Eliminating the low SNR station pairs, as well as station pairs that are separated by less than 100 km, leaves 1397 pairs from 63 stations for the velocity analysis (Figure 1). For these time series, we estimate group velocity within the 5-30 s period range using a phase-match filtering algorithm [*e.g. Cho et al., 2007*]. This algorithm estimates power-spectral density of the time series as a function of apparent velocity, and the resulting peak of the spectral density when mapped as a function of period and velocity provides the group-velocity dispersion of the dominant phase. These initial dispersion estimates are utilized to construct a synthetic matching filter for the data; the final dispersion estimates are derived from the data that has been cleaned in the time-domain using this phase-match filter. For each time series, group velocity is estimated at approximately every 1-s period between 5-30 s; the precise period for each observation is dependent on the frequency content of the data. From these data, we select all observations within a 1-s wide band at several periods: 7 s, 9 s, 15s, 17 s, 20 s, 24 s, 28 s. These periods were chosen because they span the range necessary to provide good sensitivity to crustal structure ranging from shallow sedimentary basins to the Moho, and they avoid the spectral hole between the microseism peaks, which produces unstable group-velocity estimates. While denser period sampling could be selected, little independent information would be extracted from the additional data due to the similarity of sensitivity kernels for observations of nearby periods.

The group-velocity observations provide good spatial sampling within the station network (Figure 5). In general, coverage is most dense in the northeast and mid-continent region, due to the presence of the LCSN and CNMSN stations. Coverage is relatively sparse in the west and northwest, as well as along the Gulf coast margin. At all periods, maps of the group velocity plotted at the path midpoints show good spatial coherence; in the example shown in Figure 5, low velocities associated with the sediments of the Mississippi embayment dominate the measurements in the southwest, while higher velocities indicative of hard-rock crust are prevalent in the cratonic northwest and along the Appalachian highlands. These maps are useful for identifying outliers, which can be downweighted or eliminated from the structural inversion.

The path-average group-velocity measurements are the primary data used to invert for 3D crustal velocities, as described in Section 4. As an aside, we also invert the group-velocity observations for maps of group-velocity structure at each period (Figure 6). These maps are constructed on a 0.5x0.5 degree grid, with a modest gradient smoothing operator applied. At short period (6-8 s), the spatial variability in group velocity is quite large ($\pm 15\%$), with low velocities observed along the Gulf coast, up into the Appalachian foreland basin, and within the Great Lakes region, and higher velocities found along the Appalachians, into the southern Grenville province, and along the Mid-continent arch. At longer period, the group velocities are higher with less variability, and the high velocity regions most likely reflect not only high crustal velocities (for example in the

northwest), but also relatively thin crust, for example along the Atlantic margin. Within the mid-continent region, these maps are generally consistent with those observed by *Liang and Langston* [2008], and they are also consistent on a larger scale with the continental analysis of *Benson et al.* [2007].

3. Ps Receiver Functions

Observations of Rayleigh-wave dispersion provide good constraints on lateral variations in crustal shear velocities, but they do not provide sufficient resolution to independently constrain crustal thickness (Moho depth). To attempt to address this shortcoming, we supplement the dispersion observations with a set of P-s travel times derived from receiver functions (RF) at all possible broadband stations within the study region (Figure 1).

Our analysis focused on broadband data from long-running permanent observatories east of 100°W available from the IRIS DMC. We used sites of the Global Seismic Network (network code IU), the ANSS (code US), the Lamont Cooperative Seismic Network (code LD), the New Madrid network (code NM), and the South Carolina Earth Physics project network (code SP). We selected seismograms from large ($M_w > 6.0$) events with epicentral distance less than 90°. The time window for the selection spanned 1990-2006, and best results were generally obtained from the stations that operated for relatively long duration (5 years or more) within that window. The 3-component broadband (BH) P-wave seismograms were rotated into the great-circle reference frame, high-pass filtered above 0.05 Hz, and inspected for data quality, with manual selection of high signal-to-noise events that were deemed suitable for further processing. The data were then passed through a standardized RF processing scheme based on the multitaper spectral correlation estimator of *Park and Levin* [2000].

Figures 7 and 8 provide examples of this processing scheme for two typical stations. In each, receiver functions are shown in gathers arranged by either backazimuth or epicentral distance. Individual receiver functions are binned (30° bins for backazimuth gathers, 10° bins for epicentral gathers, with 50% bin overlap) and stacked in the frequency domain. Spectral coherence between the vertical and horizontal components is used as a weight in the stack, reducing the influence of noisy spectral elements within individual RFs. Time-domain RFs are produced for a variety of spectral cutoff values. Figures 7 and 8 show RFs containing frequencies up to ~0.5 Hz (see *Levin and Park* [2000] for details of the filtering scheme).

The resulting images are used to identify the Moho converted phase Pms, and to evaluate the confidence with which we can interpret the result. Key criteria used in the evaluation are a) the continuity of candidate phase across the backazimuth gather; b) a correct sense of arrival time moveout with epicentral distance (we expect farther events to produce shorter delays of the Ps converted phase); and c) stability of the candidate phase over the frequency range.

Figure 7 provides an example of a station (WVT) at which the Moho conversion is robust. The Pms phase at ~6 s is a clear, distinct arrival on the radial component at all azimuths, and its moveout with distance is consistent with a primary P-s conversion. In contrast, Figure 8 shows an example of the station (OXF) at which the primary Moho conversion cannot be clearly identified, in this case presumably due to strong reverberations in shallow sedimentary layers.

At all stations where primary Pms phases can be identified, we stack along the primary conversion move-out curve, and measure the peak-to-peak differential time between P and Pms. This time can be interpreted as a near-vertical P-S time, and we include these observations in our inversion for crustal structure. An alternative would be to include the receiver function waveforms directly in a joint inversion with the dispersion data [e.g. *Julia et al.*, 2000, 2005]. This would potentially improve the shear-velocity constraints associated with the RFs, as the intra-crustal shear-wave multiples could be included. However, the RFs are quite variable across our study region, and confidently identifying and interpreting crustal multiples in a robust, systematic way is beyond the scope of this study. Our primary goal of including the receiver functions is to provide local estimates of vertical shear-wave travel time to better constrain crustal thickness. The travel times of the primary Pms conversions should be adequate for this purpose.

Figure 9 and Table 1 provide a summary of the P-s travel times derived from this study. To first order (assuming constant crustal velocities), these times can be interpreted in terms of crustal thickness, and the results show a clear increase in crustal thickness moving from the Atlantic margin into the continent. Of the 48 stations at which data were collected for this analysis, Ps times were estimated at 40. In order to evaluate the robustness of these estimates, we compare them to P-s times automatically measured from receiver functions by the Earthscope Automated Receiver Survey (EARS: <http://www.seis.sc.edu/projects/EARS/index.html>). The methodology of estimating the Ps time is very different, relying on constructive stacking of direct and multiply-reflected phases within the crust [*Zhu and Kanamori.*, 2000]. In general, the spatial agreement is quite good, although EARS displays a number of stations at which the Ps time appears anomalous compared to that at nearby stations. For our inversion, we utilize the Ps times measured using our more conservative manual approach.

4. 3-D models of crustal structure

We utilize the group-velocity measurements and P-s travel times to develop an improved three-dimensional shear-velocity model for the central and eastern US. The model is parameterized as simply as possible, to make it easy to implement in a wide range of wave-propagation algorithms used for source or structural modeling. It consists of three crustal layers, with an upper sedimentary layer and two hard-rock layers. The thickness of the sedimentary layer (basement depth), Moho depth, layer shear- and compressional velocities within the three layers are all spatially variable, while the intracrustal boundary is fixed at 30-km depth. Our starting model is a 3-layer average model derived from Crust 2.0 [*Mooney et al.*, 1998; *Laske et al.*, 2001] (Figure 10). Spatially, the velocities within each layer, as well as basement and Moho depth, are defined on a 0.5x0.5 degree grid.

Our data provide good constraints on the average (integrated) shear velocity within the crust, but cannot independently resolve internal layer thicknesses or compressional velocities. However, good prior knowledge exists on a number of these parameters. We constrain basement depth to match that specified in *Laske and Master's* [1997] map of sediment thickness. P velocities are tied to the shear velocities through a depth-dependent P/S ratio consistent with lithological changes through the crustal column [*Mooney et al.*, 1998]. Specifically, v_p/v_s are constrained to values of 1.98, 1.75, and 1.82 within the sediment layer, middle crust, and lower crust, respectively.

The group-velocity data provide the primary constraint on crustal shear velocities, and the sensitivity kernels for these observations are calculated numerically from the modal eigenfrequency kernels [Rodi *et al.*, 1975] at the center period of each observation (Figure 11). At the shortest periods, the data are quite sensitive to the structure of the upper and middle crust, while longer-period observations provide increased sensitivity to the lower crust. We calculate group-velocity sensitivity to basement and Moho depth in the same manner. For the P-s vertical travel times, the sensitivity to v_p and v_s within each layer, as well as the boundary depths, are calculated analytically.

We inverted the observations using a damped, linearized least-squares inversion, with a spatial smoothness constraint. We tested a range of choices for spatial smoothness both velocity space and in discontinuity topography, with a goal of finding a model that provided an acceptable goodness of fit to the data, while also providing a velocity structure that will be useful for synthetic modeling of regional source properties. We found it necessary to tightly constrain two aspects of the model space. First, we largely use the sediment thickness variations to fit the short-period data, and keep the sediment-layer shear velocity close to a starting value. Releasing this parameter resulted in large perturbations to shallow velocity structure that trade off strongly with sediment thickness. Second, we attempted to keep a positive velocity gradient with depth, with the mid-crust layer remaining at a lower velocities than the lower crustal layer. This goal is largely attained, although there is a region in the middle of the model space where the data consistently require models that have very high mid-crustal velocities. Damping these velocities resulted in significant increase in the misfit to the data, and so the presented model has this feature. This may limit the utility of the model for some applications.

Our preferred model is presented in Figure 12. Basement depth ranges from 0-13 km, while Moho depth varies from 26-50 km. The thickest sediment package and the thinnest crust are found along the Atlantic and Gulf margins. In places where Moho depth is less than 30 km, the crust contains only two layers, with the thickness of layer 3 being zero. The sediment layer is effectively zero thickness in cratonic portions of the North American interior. Shear velocities in the sediment layer are approximately 1580 m/s, while shear velocities in the middle and lower crust average approximately 3710 and 3900 m/s, respectively. The spatial variations are dominated by a belt of high velocity middle crust that extends down the axis and westward of the Appalachians; lower crust in this region is not particularly high velocity, producing a crustal velocity profile that has a less steep (even negative) gradient with depth.

This model strikes a balance between fitting the data, and still providing a smooth, simple structure that will be useful for source modeling. Variance reduction of the group-velocity data is just over 60%; a slightly improved fit could be achieved, but the resulting models have very rapid and large spatial fluctuations in velocity that are probably not physical. Interestingly, the model does not do well in fitting the receiver-function data. This appears to be because the RF data simply show too much short-scale length variance (presumably due to local basin structure) to be well fit by our smooth model. We continue to explore ways to better incorporate RF data in the modeling.

The model is available for download at http://www.ldeo.columbia.edu/~gaherty/ceus_model. It is stored in a simple ascii format, with the following parameters specified at 0.5x0.5 degree intervals: depth of basement, mid-crustal discontinuity, and the Moho; and three layers of shear and compressional

velocities bounded by these discontinuities. This model can be easily adapted for general use.

5. Summary

We present three-dimensional models of crustal structure for the central and eastern United States (CEUS), east of 100°W longitude. These 3D wavespeed models are derived from 72 stations of the Advanced National Seismic System (ANSS), using two types of data: (1) Rayleigh waveforms in the period range 8-30 s propagating between all possible pairs of stations in the region, generated through cross-correlation of ground-motion noise (so-called ambient-noise Green's functions); and (2) converted-phase (receiver-function) measurements beneath approximately the same set of broadband seismic stations, which provide localized estimates of integrated velocity structure between the surface and Moho beneath each station. We constructed ambient-noise Green's functions from one year of data, producing Rayleigh waveforms for nearly 1500 receiver-receiver paths with sufficient signal-to-noise ratio (> 5) for group-velocity analysis. We inverted nearly 1500 Rayleigh-wave group velocities and P_s receiver functions for over 45 stations for a crustal model with P and S velocities defined in three layers (sediment, upper crust, and lower crust) on a 0.5x0.5 degree grid, using an averaged version of model Crust 2.0 as a starting model. Basement depth ranges from 0-13 km, while Moho depth varies from 26-50 km. Shear velocities in the sediment layer are approximately 1580 m/s, while shear velocities in the middle and lower crust average approximately 3710 and 3900 m/s, respectively. This simply parameterized and highly flexible model characterizes lateral variations in crustal structure within the CEUS in a form that is useful for earthquake source studies. The new model is available to the earthquake modeling community through the website for the Lamont Doherty Earth Observatory, at http://www.ldeo.columbia.edu/~gaherty/ceus_model.

References

- Ammon, C.J, R.B. Herrmann, C.A. Langston, and H. Benz, Faulting parameters of the January 16, 1994 Wyoming Hills, PA earthquakes, *Seism. Res. Lett.*, 69, 261-269, 1998.
- Bensen, G.D., M.H. Ritzwoller, M.P. Barmin, A.L. Levshin, F. Lin, M.P. Moschetti, N.M. Shapiro, and Y. Yang, Processing seismic ambient noise data to obtain reliable broad-band surface wave dispersion measurements, *Geophys. J. Int.*, 169, 1239-1260, doi: 10.1111/j.1365-246X.2007.03374.x, 2007.
- Chen, P., L. Zhao and T. H. Jordan, Finite Moment Tensor of the 3 September 2002 Yorba Linda Earthquake, *Bull. of Seism. Soc. of Am.*, 95, 1170-1180, 2005.
- Chen, P., L. Zhao and T. H. Jordan, Full 3D Tomography for Crustal Structure of the Los Angeles Region, *Bull. of Seism. Soc. of Am.*, 97, 1094-1120, doi: 10.11785/0120060222, 2007.
- Chen, P., L. Zhao and T. H. Jordan, Resolving fault-plane ambiguity for small earthquakes, *Bull. of Seism. Soc. of Am.*, submitted, 2008.
- Cho, K. H., R. B. Herrmann, C. J. Ammon and K. Lee (2006), Imaging the Upper Crust of the Korean Peninsula by Surface-Wave Tomography, *Bull. Seism. Soc. Am.*, 97, 198 - 207, 2007.

- Dalton, C.A., J.B. Gaherty, and A.M. Courtier, Crustal VS structure in northwestern Canada: Imaging the Cordillera-craton transition with ambient-noise tomography, *J. Geophys. Res.*, *in press*, 2011.
- Dreger, D.S., and D.V. Helmberger, Determination of source parameters and regional distances with single station or sparse network data, *J. Geophys. Res.*, *98*, 8107-8125, 1993.
- Du, W.-X., W.-Y. Kim, and L.R. Sykes, Earthquake source parameters and state of stress for the northeastern United States and southeastern Canada from analysis of regional seismograms, *Bull. Seism. Soc. Amer.*, *93*, 1633-1648, 2003.
- Dziewonski, A.M., T.-A. Chou, and J.H. Woodhouse, Determination of earthquake source parameters from waveform data for studies of global and regional seismicity, *J. Geophys. Res.*, *86*, 2825-2852, 1981.
- Harmon, N., D. Forsyth, and S. Webb, Using ambient seismic noise to determine short-period phase velocities and shallow shear velocities in young oceanic lithosphere, *Bull. Seism. Soc. Am.*, *97*, 2009-2023, doi: 10.1785/ 0120070050, 2007.
- Julia, J., C.J. Ammon, R.B. Herrmann, and A.M. Correig, Joint inversion of receiver function and surface wave dispersion observations, *Geophys. J. Int.*, *143*, 1-19, 2000.
- Julia, J., Ammon, C. J. and Nyblade, A. A., Evidence for mafic lower crust in Tanzania, East Africa, from joint inversion of receiver functions and Rayleigh wave dispersion velocities, *Geophys. J. Int.*, *162*, 555-569, doi:10.1111/j.1365-246X.2005.02685.x, 2005.
- Kim, W.-Y., The 18 June 2002 Caborn, Indiana, Earthquake: Reactivation of ancient rift in Wabash Valley seismic zone?, *Bull. Seismol. Soc. Amer.*, *93*, 2201-2211, 2003.
- Laske, G. and G. Masters, A Global Digital Map of Sediment Thickness, *EOS Trans. AGU*, *78*, F483, 1997.
- Laske, G., G. Masters, and C. Reif, 2001. CRUST 2.0, A New Global Crustal Model at 2x2 Degrees, <http://mahi.ucsd.edu/Gabi/rem.html>.
- Levin V., and J. Park, P-SH conversions in layered media with hexagonally symmetric anisotropy: A CookBook, *Pure Appl. Geoph.*, *151*, 669-697, 1998.
- Liang, C. and C.A. Langston, Ambient seismic noise tomography and structure of eastern North America, *J. Geophys. Res.*, *in press*, 2008.
- Ligorria, J.P., and Ammon, C.J, Iterative deconvolution and receiver-function estimation: *Bull. Seism. Soc. Amer.*, *89*, 1395-1400, 1999.
- Maceira, M., C.J. Ammon, and R.B. Herrmann, Faulting parameters of the September 25, 1998 Pymatuning, PA earthquake, *Seism. Res. Lett.*, *71*, 742-752, 2000.
- Magistrale, H., S. Day, R.W. Clayton, and R. Graves, The SCEC Southern California reference Three-dimensional seismic velocity model version 2, *Bull. Seism. Soc. Amer.*, *90*, S65-S76, 2000.
- Mooney, W.D., G. Laske, and T.G. Masters, CRUST 5.1: A global crustal model at 5x5 degrees, *J. Geophys. Res.*, *103*, 727-748, 1998.
- Park-J., and V. Levin, Receiver functions from multiple-taper spectral correlation estimates, *Bull. Seism. Soc. Amer.*, *90*, 1507-1520. 2000.
- Pasyanos, M.E., D.S. Dreger, and B. Romanowicz, Towards real-time estimation of regional moment tensors, *Bull. Seism. Soc. Amer.*, *86*, 1255-1269, 1996.
- Ritsema, J. and T. Lay, Rapid source mechanism determination of large earthquake sin the western US, *Geophys. Res. Lett.*, *20*, 1611-1614, 1993.

- Rodi, W.L., P. Glover, T.M.C. Li, and S.S. Alexander, A fast, accurate method for computing group velocity partial derivatives for Rayleigh and Love modes, *Bull. Seismol. Soc. Am.*, 65, 1105–1114., 1975.
- Shapiro, N.M. and M. Campillo, Emergence of broadband Rayleigh waves from correlations of ambient seismic noise, *Geophys. Res. Lett.*, 31, L07614, doi:10.1029/2004GL019491, 2004.
- Shapiro, N.M., M. Campillo, L. Stehly, and M.H. Ritzwoller, High-resolution surface-wave tomography from ambient seismic noise, *Science*, 307, 1615-1618, 2005.
- Zhao, L.S. and D.V. Helmberger, Source estimation from broad-band regional seismograms, *Bull. Seism. Soc. Am.*, 84, 91-104, 1994.

Table 1. Estimates of Pms time values at sites in Eastern North America. At sites where Pms column contains an X the value cannot be measured from receiver functions.

site	net	latitude	longitude	Pms, sec	quality
CCM	IU	38.06	-91.24	5.5	2
HKT	IU	29.96	-95.84	3.8	5
HRV	IU	42.51	-71.56	3.1	2
SSPA	IU	40.64	-77.89	4.3	4
WCI	IU	38.23	-86.29	5.4	2
WVT	IU	36.13	-87.83	5.5	1
AAM	US	42.30	-83.66	6.0	5
ACSO	US	40.23	-82.98	5.5	2
BINY	US	42.20	-75.99	4.6	1
BLA	US	37.21	-80.42	4.8	2
CBN	US	38.20	-77.37	X	
JFWS	US	42.91	-90.25	5.0	3
LBNH	US	44.24	-71.93	4.4	2
LONY	US	44.62	-74.58	5.9	3
LRAL	US	33.03	-87.00	4.5	4
LSCT	US	41.68	-73.22	3.4	3
MCWV	US	39.66	-79.85	4.5	3
MIAR	US	34.55	-93.58	5.9	2
MYNC	US	35.07	-84.13	6.2	4
NATX	US	31.76	-94.66	X	
OXF	US	34.51	-89.41	X	
TZTN	US	36.54	-83.55	5.8	3
YSNY	US	42.48	-78.54	5.5	2
ACCN	LD	43.38	-73.67	5.5	1
ALLY	LD	41.65	-80.14	5.7	4
FMPA	LD	40.05	-76.32	5.0	5
FOR	LD	41.01	-73.91	3.6	3
MVL	LD	40.00	-76.35	5.0	2
PAL	LD	41.01	-73.91	4.0	4
SDMD	LD	39.41	-76.84	3.4	1
PRNY	LD	42.47	-76.54	5.2	3
AGBLF	SP	33.40	-81.76	3.7	2
BBLV	SP	33.92	-81.53	3.8	1
CLINT	SP	34.48	-81.86	4.2	5
DWDAN	SP	34.74	-82.83	5.8	3
TIMBR	SP	33.34	-79.89	X	
WOAK	SP	34.62	-83.05	X	
BLO	NM	39.17	-86.52	6.0	2
FVM	NM	37.98	-90.43	5.8	3
MPH	NM	35.12	-89.93	X	
OLIL	NM	38.73	-88.10	6.0	1
PLAL	NM	34.98	-88.08	5.5	3
PVMO	NM	36.41	-89.70	X	
SIUC	NM	37.71	-89.22	2.7	1
SLM	NM	38.64	-90.24	6.3	2
UALR	NM	34.78	-92.34	4.5	3
UTMT	NM	36.34	-88.86	X	

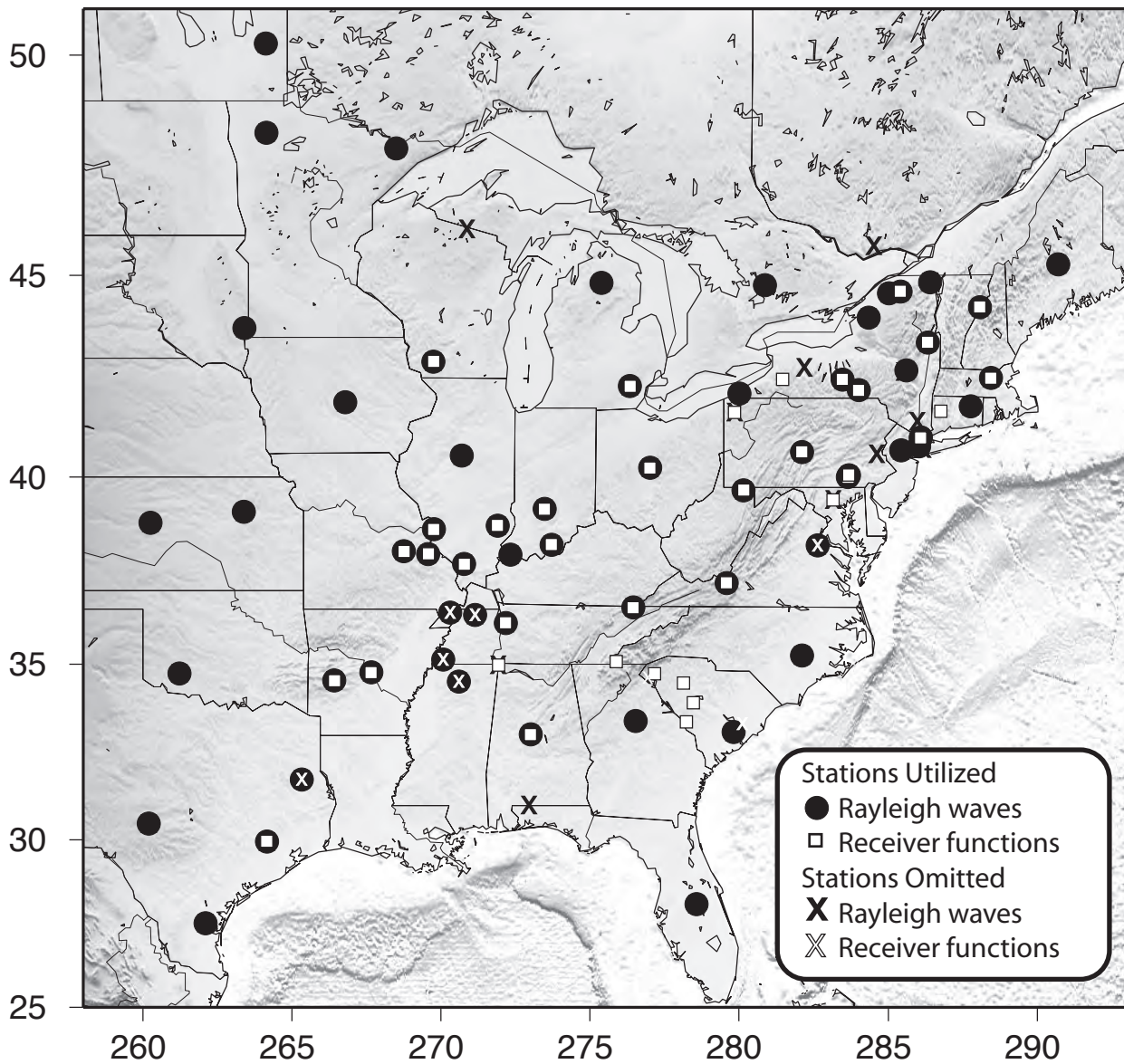


Figure 1. Map of ANSS and CNSN broadband seismic stations analyzed. Circles indicated stations used to estimate Rayleigh-wave group velocities, while open squares mark those stations where P-s times were successfully extracted from the receiver functions. Black X's indicate stations that were collected for the group-velocity analysis, but were omitted due to low signal-to-noise of the year-long stacks. White X's mark stations where receiver-function analysis did not produce a robust estimate of P-s time.

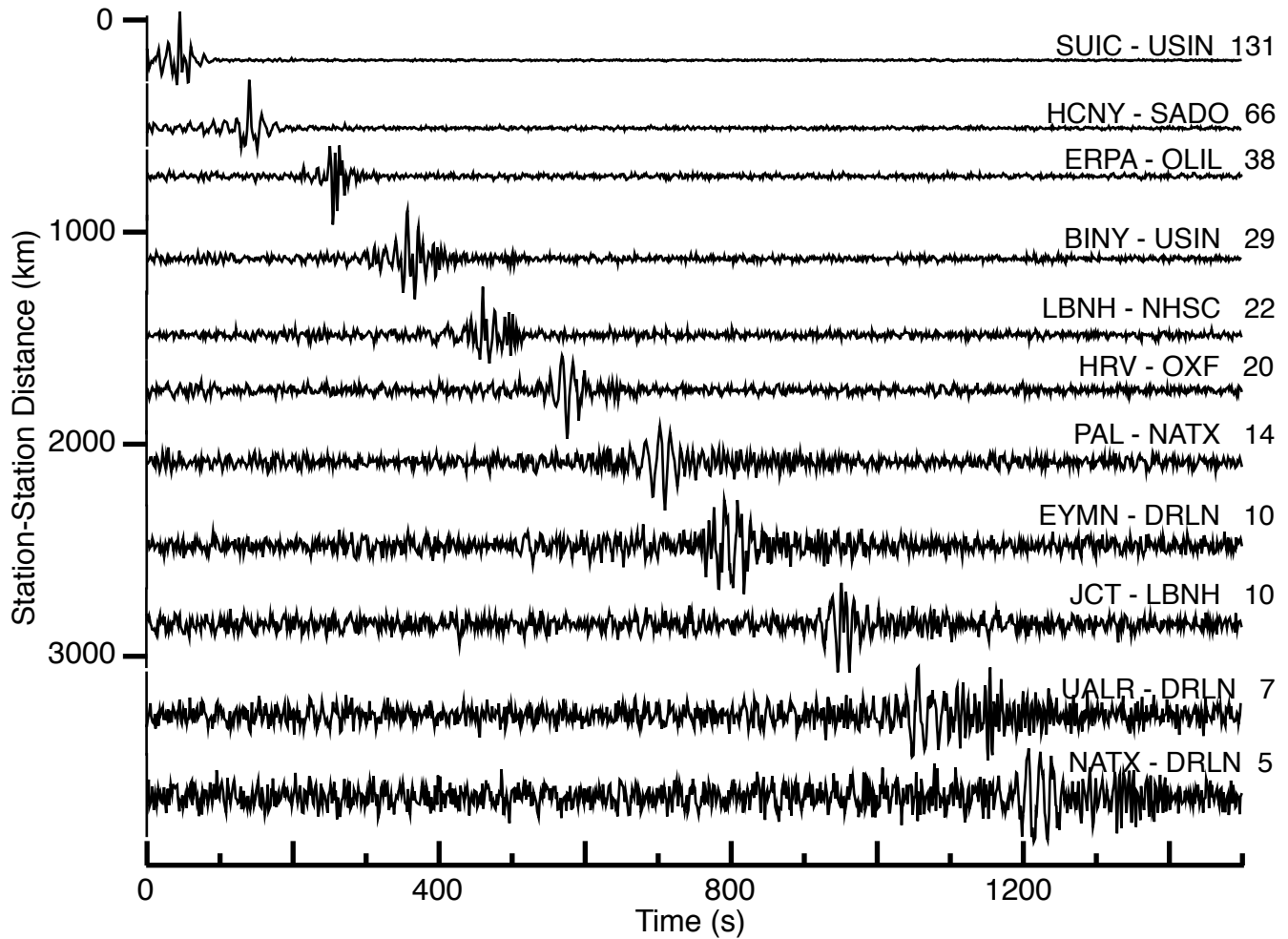


Figure 2. Examples of year-long stacks of broadband (5-100 s) ground displacement cross-correlation functions. Time series represents the average of the causal and acausal correlation function, and are plotted as a function of interstation distance. Examples represent a range of signal to noise ratio, indicated to the right of each trace.

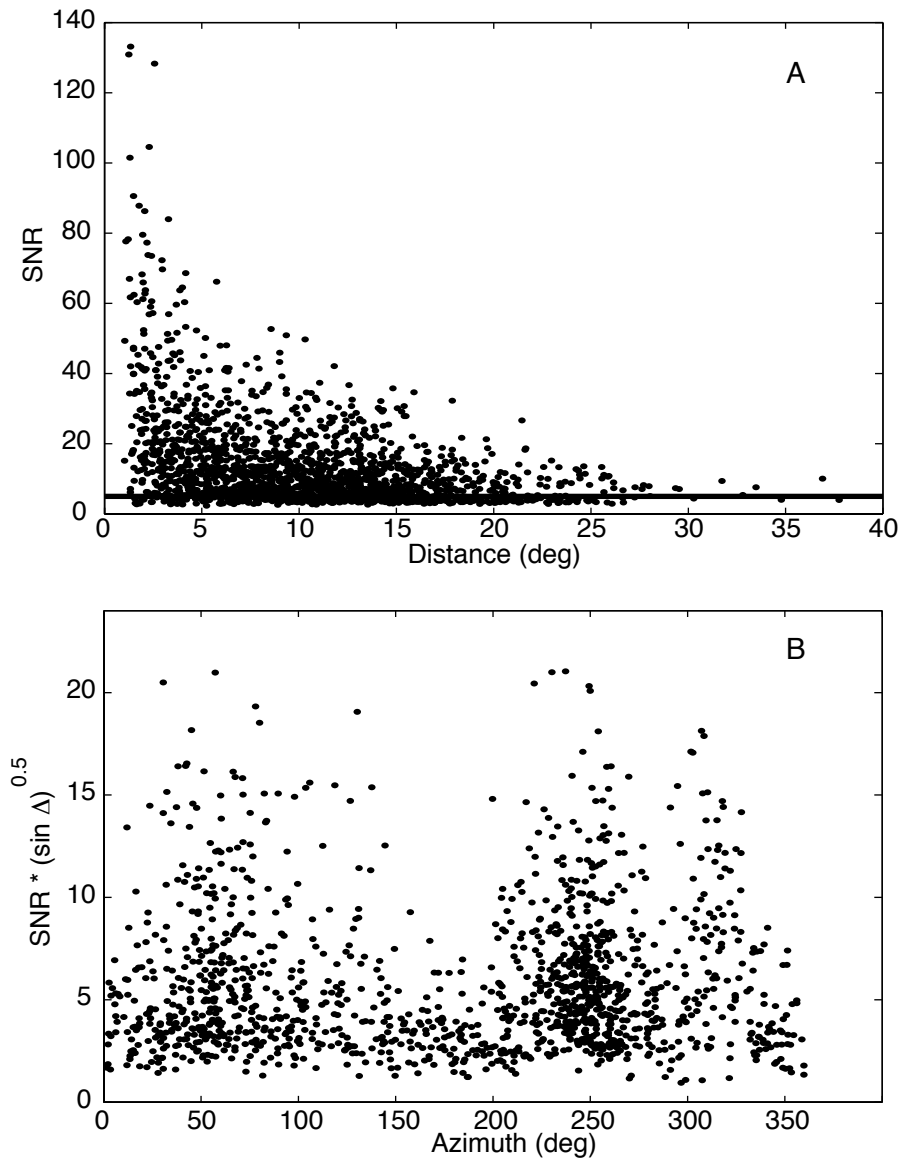


Figure 3. (a) Signal-to-noise ratio (SNR) of broadband year-long cross-correlation functions, plotted as a function of interstation distance. Horizontal line defines SNR = 5 cutoff. (b) SNR corrected for surface-wave geometrical spreading [Stein and Wysession, 2003], plotted as a function of interstation azimuth.

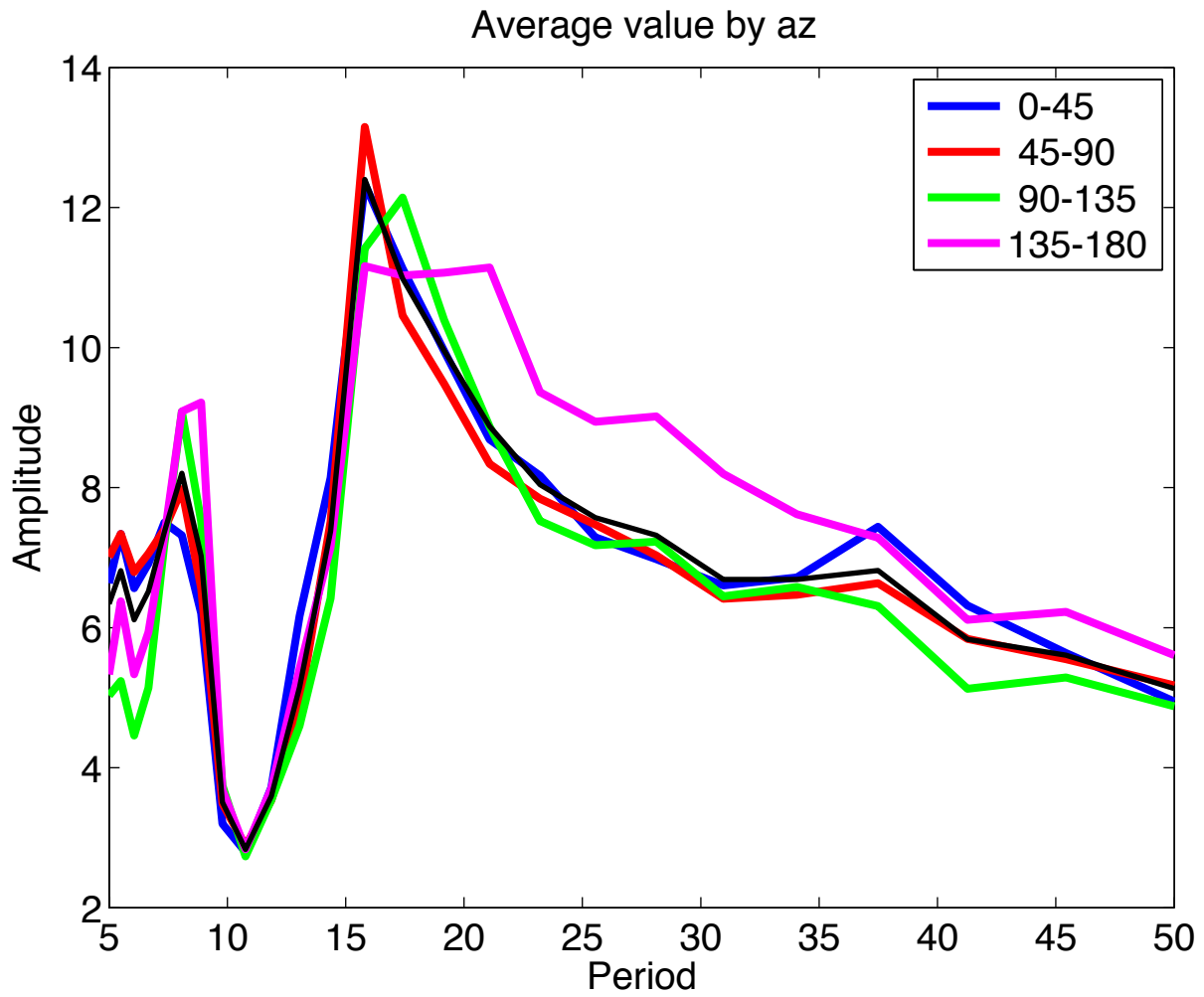


Figure 4. Amplitude spectra for the stacked correlation functions, averaged in bands of interstation azimuth. Strong peaks associated with the microseism are clear. Observations within the spectral hole at ~12 s period are omitted from the analysis.

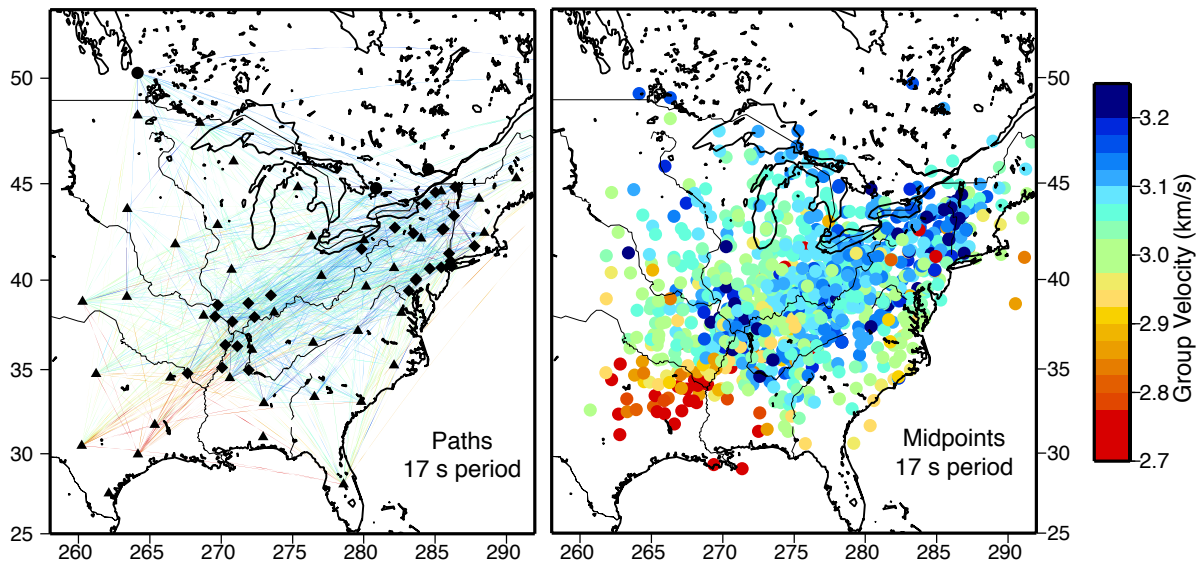


Figure 5. Examples of the spatial coverage and data consistency of interstation ambient-noise cross-correlation functions. Left panel displays group velocities measured at 17 s period, projected onto the raypath between each station. Right panel shows the same observations plotted at the midpoint of each station pair. In both projections, the general spatial consistency of the group velocity observations is clear, and the regions of best spatial coverage can be discerned.

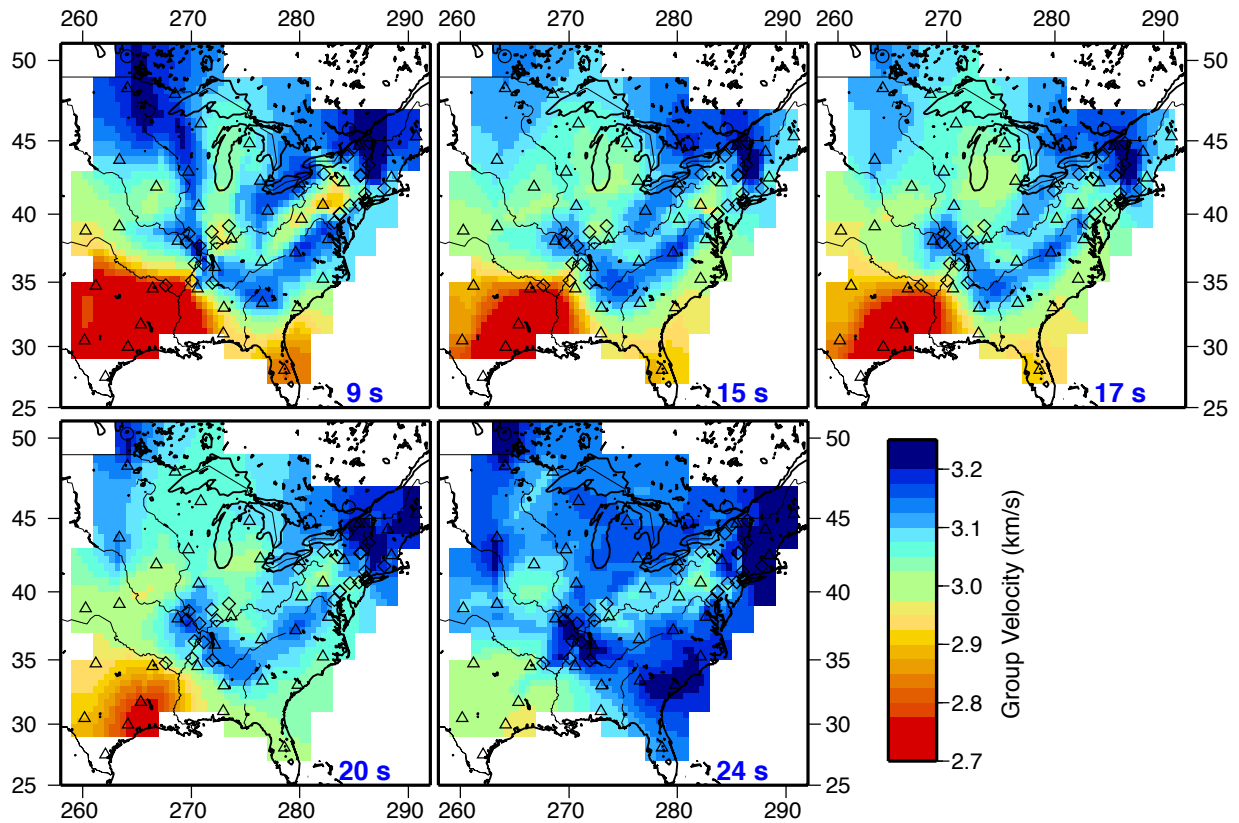


Figure 6. Spatial variations in group velocity estimated from inversion of interstation group velocity estimates. Maps are presented for periods of 9 s, 15 s, 17 s, 20 s, and 24 s, as indicated in the lower right corner of each panel. The maps are dominated by the low-velocity sedimentary basin beneath Texas and the Gulf Coast, contrasting with the high-velocity crust found in the northern mid-continent and beneath the northern Appalachians. Velocities systematically increase with increasing period due to increase in sampling depth.

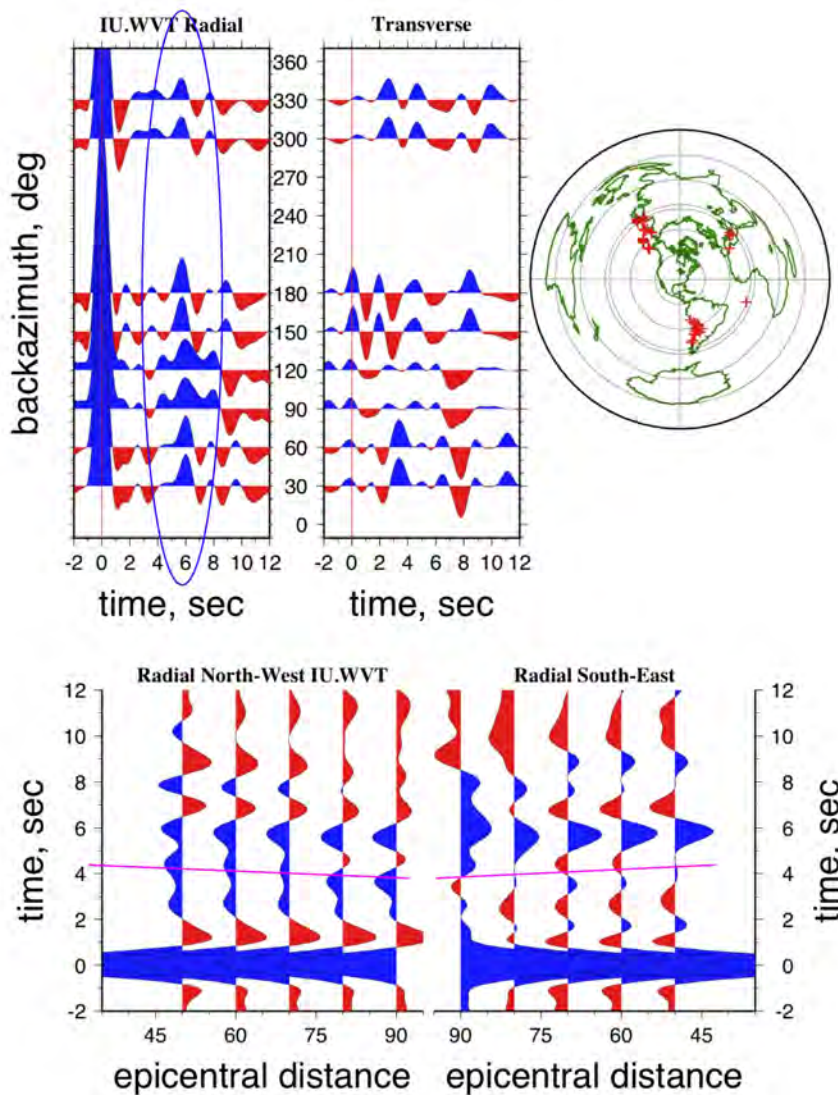


Figure 7. Example of receiver function analysis for a station with a high-quality Moho conversion. Top left panels shows receiver-function stacks for events shown in global map, organized as a function of back-azimuth for both radial and transverse components. Distinct, well-isolated arrival at ~6 sec is interpreted as a direct P-s conversion at the Moho, and the timing of this arrival relative to direct P, and corrected to zero offset, is used as a direct constraint in the inversion for velocities and crustal thickness. Bottom panel shows stacks in two back-azimuth bands plotted as a function of epicentral distance, which provides further evidence that the moveout behavior is consistent with a primary Moho conversion.

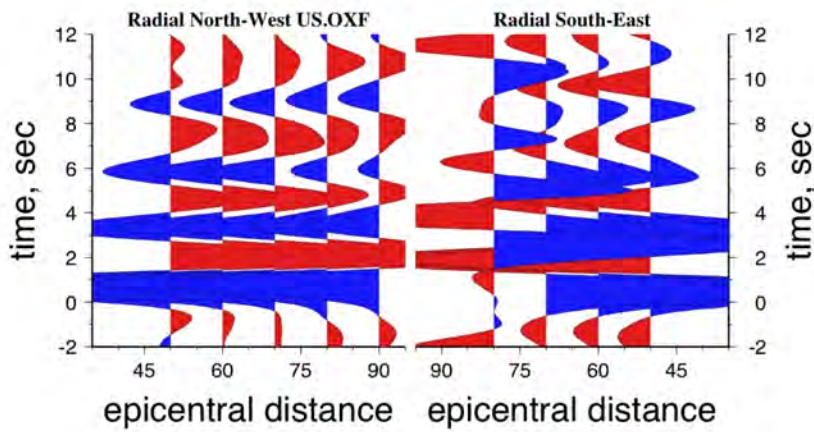
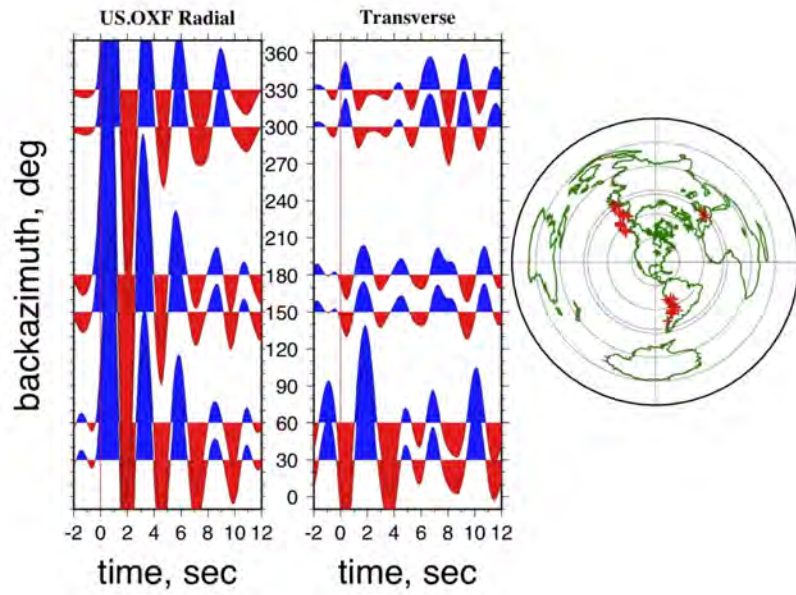


Figure 8. Example of a receiver function that shows a large degree of ringing, presumably in sedimentary layers in the shallow crust. Moho conversions cannot be confidently identified on either the back-azimuthal or epicentral distance stacks, and thus a P-s estimate is not produced for this station.

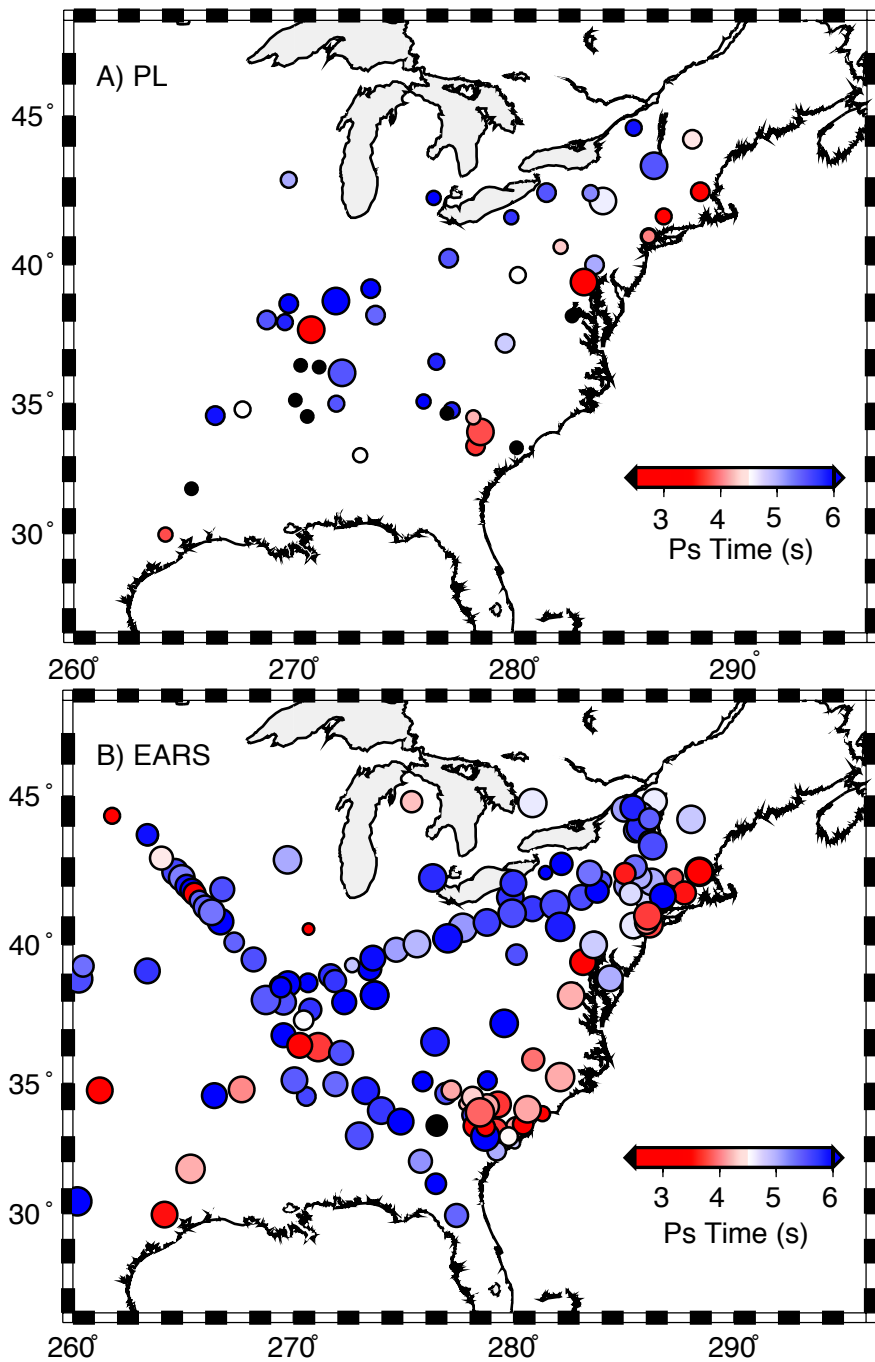


Figure 9. Estimate of one-way P-s vertical travel time plotted at each station location. (a) P-s times estimated using our application of the Park and Levin (PL) analysis, as described in section 3. (b) P-s times calculated from crustal-thickness estimates obtained through the on-line automated receiver function processing EARS. EARS provides travel times at many stations where the PL analysis did not produce a stable result (see Figure 8), as well as short-term stations that were not considered in our analysis. EARS results have not undergone careful quality control, however, and we opt not to include them in our analysis.

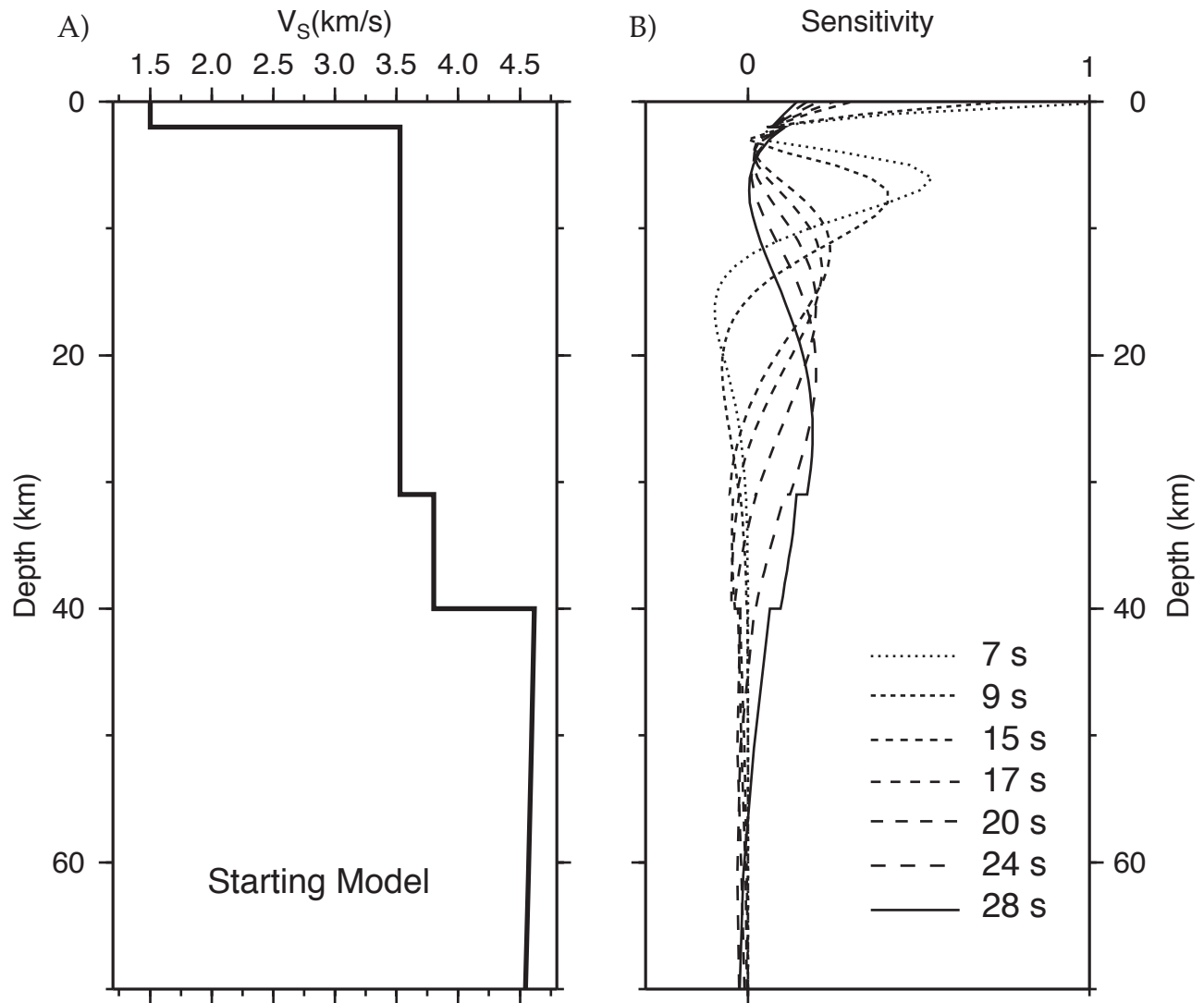


Figure 10. (a) One-dimensional shear velocity model that is used as the starting model for the inversion. Model consists of a sedimentary layer with variable-depth basement, a middle crustal layer with a base fixed at 30 km, and a lower crust with variable-depth Moho. (b) Sensitivity kernels for group velocity measurements at periods ranging from 7 to 28 s. Short-period kernels are strongly peaked at shallow depth, while longer-period kernels are sensitive to the entire crustal column. At these periods, there is little sensitivity to mantle structure. Kernels are normalized relative to the 7-sec kernels, which displace maximum sensitivity in this depth interval.

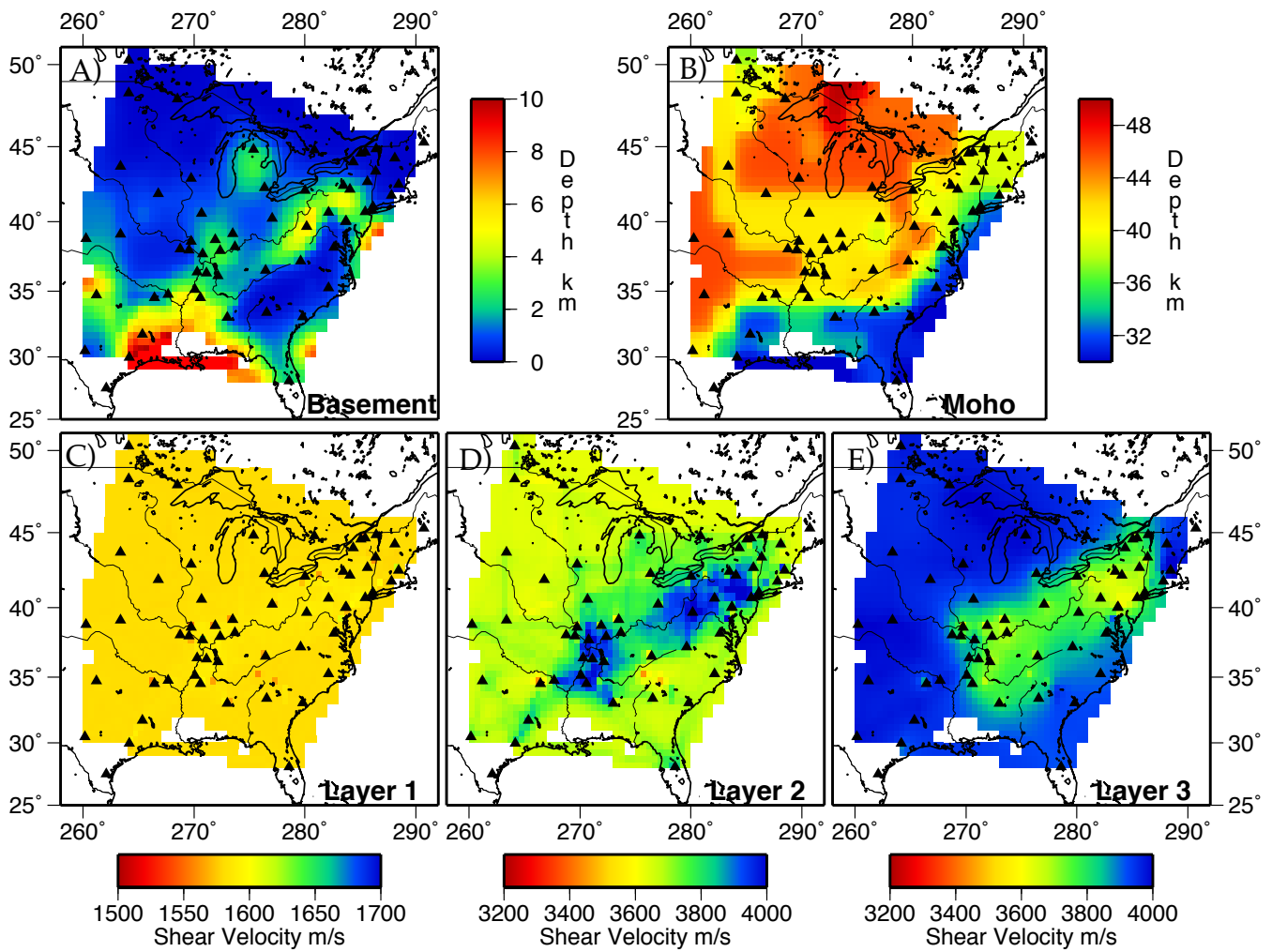


Figure 11. Final crustal shear velocity model for central and eastern North America. Figure presents lateral variations in (a) basement depth; (b) Moho depth; (c) sediment layer velocities; (d) mid-crustal velocities; and (e) lower crustal velocities. P velocity variations are estimated by maintaining the depth-dependent V_p/V_s ratio that is found in the starting 1D model.